Molecularly distinct cores coexist inside stress granules

Luca Cirillo[1,3*], Adeline Cieren [1,3], Monica Gotta[1,2,4,*]

1 Department of Cellular Physiology and Metabolism, Faculty of Medicine, University of Geneva, 1211 Geneva 4, Switzerland

2 Swiss National Centre for Competence in Research Program Chemical Biology, 1211 Geneva, Switzerland.

3 Co-first author

4 Lead Contact

* Corresponding author

Correspondence

luca.cirillo@unige.ch (L.C.),

monica.gotta@unige.ch (M.G.)

19 **Summary**

20 Stress granules are membraneless organelles that form in eukaryotic cells after stress
21 exposure. Stress granules are constituted by a stable core and a dynamic shell that
22 establishes a liquid-liquid phase separation with the surrounding cytosol. The structure and
23 assembly of stress granules and how different components contribute to their formation are
24 not fully understood. Here, using super resolution and expansion microscopy, we find that
25 the stress granule component UBAP2L and the core protein G3BP1 occupy different
26 domains inside stress granules. Since UBAP2L displays typical properties of a core protein,
27 our results indicate that different cores coexist inside the same granule. Consistent with a
28 role as a core protein, UBAP2L is required for stress granule assembly in several stress
29 conditions and reverse genetics show that it acts upstream of G3BP1. We propose a model
30 in which UBAP2L is an essential stress granule nucleator that facilitates G3BP1 core
31 formation and stress granule assembly and growth.

32

33   INTRODUCTION

34   Eukaryotic cells have evolved a series of mechanisms to counterbalance external stresses

35   that may pose a threat to their internal homoeostasis. One of these mechanisms is the

36   inhibition of protein translation and the consequent formation of membraneless organelles

37   known as stress granules (Kedersha et al., 2000; reviewed in Mahboubi and Stochaj, 2017;

38   Panas et al., 2016; Protter and Parker, 2016). Following translation inhibition, polysomes

39   disassemble releasing 48S preinitiation complexes (PICs). In the cytosol, mRNA, PICs and

40   other proteins coalesce in stress granule cores (Kedersha et al., 2000). Stress granule cores

41   recruit a shell, whose properties are dominated by weak interactions between proteins and

42   RNAs (Jain et al., 2016; Treeck et al., 2018; Wheeler et al., 2016). The stress granule shell

43   establishes a liquid-liquid phase separation with the surrounding cytoplasm, explaining the

44   high dynamicity of stress granule components (Han et al., 2012; Kato et al., 2012; Weber

45   and Brangwynne, 2012). A mature stress granule will be formed by a phase separated shell

46   surrounding several stable cores (Jain et al., 2016). However, the identity of the stress

47   granule cores, their formation and localization pattern within the granules remain

48   incompletely understood.

49   Proteins that contribute to the formation of stress granules include G3BP1 and 2 (Ras

50   GTPase-activating protein-binding protein 1 and 2), TIA-1 (T-cell-restricted intracellular

51   antigen-1), TIAR (TIA-1-related), TTP (Tristetraprolin) and FMRP (Fragile X mental

52   retardation protein 1 homolog) (Kedersha et al., 2000; Mazroui et al., 2002; Stoecklin et al.,

53   2004; Tourrière et al., 2003). Although the composition of stress granules as well as the

54   requirement for specific proteins vary according to the stress-inducing agent and cell type

55   (Aulas and Vande Velde, 2015; Bounedjah et al., 2014; Markmiller et al., 2018), G3BP1 and

56   2 have been shown to be required for stress granule nucleation in most cases (Kedersha et

57   al., 2016; Matsuki et al., 2013) and G3BP1 is highly enriched in stress granule cores (Jain

58   et al., 2016; Markmiller et al., 2018; Wheeler et al., 2016; Youn et al., 2018). The relative

59   stability of stress granule cores has recently allowed their purification and the identification

60   of novel stress granule nucleators, among them the protein UBAP2L (Ubiquitin-associated

61   protein 2-like (Markmiller et al., 2018; Youn et al., 2018). UBAP2L is a ubiquitous and

62   abundant protein in human tissues (Beck et al., 2011; Lonsdale et al., 2013; Melé et al.,

63   2015; Uhlén et al., 2015), it promotes cancer progression and metastasis (Aucagne et al.,

64   2017; Chai et al., 2016; He et al., 2018; Li and Huang, 2014; Li et al., 2018; Ye et al., 2017,

65   p. 20; Zhao et al., 2015) and may be involved in neurodegenerative diseases (Markmiller et

66 al., 2018). Despite its abundance and potential implication in diseases, the exact role of

67 UBAP2L in cell physiology and stress granule formation is not yet understood.

68 Here, we used a combination of cell biology and reverse genetics to investigate the role of

69 UBAP2L is stress granule formation. We showed that UBAP2L is present in discrete

70 particles inside stress granules, which do not colocalize with G3BP1 stress granule cores.

71 UBAP2L acts upstream of G3BP1 and 2 in stress granule assembly but does not interfere

72 with stress-induced translational inhibition, indicating that UBAP2L is a crucial stress granule

73 nucleator downstream of translational inhibition. Our results show that molecularly distinct

74 stress granule cores coexist in the same stress granules.

75

76　RESULTS

77　**UBAP2L localizes inside stress granules in discrete particles distinct from G3BP1**

78　**cores.**

79　Given the importance of UBAP2L in sodium arsenite (arsenite hereafter)-induced stress

80　granule assembly (Markmiller et al., 2018; Youn et al., 2018), we sought to investigate its

81　sublocalization inside stress granules. To this end, we used 3D-STED (3D Stimulated

82　Emission Depletion miscroscopy, Hell and Wichmann, 1994; Klar and Hell, 1999). 3D-STED

83　immunofluorescence of HeLa K cells fixed and stained with anti-UBAP2L antibodies,

84　revealed that each stress granule is formed by discrete UBAP2L particles of roughly round

85　shape (Fig. 1 A), with a diameter of 187.0 ± 44.2 nm (mean ± SD, Fig. 1 B). We also

86　performed 3D-STED on HeLa K cells stained for the known stress granule component

87　G3BP1 and measured the diameter of G3BP1 cores (Fig. 1 A). Our analysis revealed a

88　diameter of 182.7 ± 41.9 nm (mean ± SD), which is in good agreement with the published

89　diameter of 190.8 ± 28.3 nm (Fig. 1B, Jain et al., 2016). The number of UBAP2L and G3BP1

90　particles linearly correlated with the stress granule volume (Fig. S1 A). The localization of

91　UBAP2L in discrete particles and their size distribution suggest that UBAP2L localizes to

92　stress granule cores.

93　The shell and the core of stress granules do not only differ in their composition, but also in

94　the dynamics of their components, with core proteins being more stable and shell proteins

95　more dynamic. To assess whether UBAP2L particles are stress granule cores, we measured

96　the dynamics of UBAP2L in living cells. To visualize UBAP2L, we tagged endogenous

97　UBAP2L at the C-terminus with the red fluorescent protein mScarlet using CRISPR-Cas9

98　(Fig. S1 B Bindels et al., 2017). Clones were screened via PCR (Polymerase Chain

99　Reaction, Fig. S1 C) and validated with western blot using an anti-UBAP2L antibody (Fig.

100　S1 D). In addition, treatment of UBAP2L-mScarlet HeLa cells with a siRNA directed against

101　mScarlet, followed by western blot analysis, confirmed the successful insertion of the

102　construct (Fig. S1 E). Although we failed to identify a homozygous insertion (Fig. S1 D, E),

103　live cell imaging revealed that UBAP2L-mScarlet transitions from a diffuse cytosolic signal

104　to a droplet-like pattern following arsenite exposure (Fig. S1 F). This observation is

105　consistent with published immunofluorescence of UBAP2L (Markmiller et al., 2018; Youn et

106　al., 2018), indicating that UBAP2L-mScarlet recapitulates the localization of wild-type

107　UBAP2L. Having created a tool to visualize UBAP2L *in vivo*, we next measured the

108　dynamics of UBAP2L in stress granules using Fluorescence Recovery after Photobleaching

109　(FRAP). After treating UBAP2L-mScarlet HeLa cells with arsenite to induce stress granule

110 formation, we bleached a single cytosolic granule and followed the fluorescence recovery
111 over time using confocal microscopy (Fig. 1 C). Analysis of fluorescence recovery for 3
112 minutes after bleaching, highlighted the presence of a slow recovery fraction of UBAP2L-
113 mScarlet (Immobile Fraction = 18.2 ± 1.9 %, mean ± SD, Fig. 1 D, Fig. S1 G, H). To validate
114 the presence of a slow recovery fraction we repeated the bleaching cycle in the same stress
115 granule in the context of a double FRAP experiment (Krouwels et al., 2005; Stavreva and
116 McNally, 2004). If the first photobleaching event bleaches all the fluorophores of the
117 immobile fraction, the recovery curve after the second bleaching of the same granule
118 depends uniquely on the mobile fraction and should yield a 100% recovery. We obtained a
119 complete recovery of the fluorescence 3 minutes after the second bleaching (Immobile
120 Fraction = -0.05 ± 2.1 %, mean ± SD, Fig. 1 D, Fig. S1 G, H). Moreover, the second recovery
121 curve is significantly different from the first recovery curve (p<0.0001, two-way ANOVA).
122 This experiment demonstrates that UBAP2L-mScarlet exists in stress granules in at least
123 two different pools, characterized by different diffusivity, in agreement with previous data on
124 other stress granule proteins (Jain et al., 2016) and mRNAs (Mollet et al., 2008; van der
125 Laan et al., 2012).

126 The localization in discrete particles and the presence of an immobile fraction suggest that
127 UBAP2L behaves as stress granule core protein. We therefore, asked whether UBAP2L
128 particles colocalize with G3BP1. We performed two-colors 2D STED on arsenite-treated
129 HeLa K cells fixed and stained with both anti-UBAP2L and anti-G3BP antibodies. Contrary
130 to our expectations, most UBAP2L and G3BP1 stress granule particles did not colocalize
131 (Fig. 1 E, F, Pearson correlation coefficient: 0.01 ± 0.25, mean ± SD). To confirm these
132 observations, we investigated the localization of UBAP2L with an independent approach.
133 Ultrastructure Expansion Microscopy (U-ExM) allows imaging beyond the resolution limits
134 of visible light by expanding the sample without affecting its ultrastructure (Gambarotto et
135 al., 2019). We performed U-ExM on arsenite-induced stress granules in Hela K cells fixed
136 and stained with antibodies against UBAP2L and G3BP1. With an estimated expansion
137 between 3.5 and 4.0-fold compared to unexpanded samples, three-dimensional confocal
138 microscopy revealed that UBAP2L and G3BP1 localize in discrete patterns inside stress
139 granules (Fig. 1 G, H, I), supporting our 3D-STED results (Fig. 1 A). In addition, in agreement
140 with 2D-STED (Fig. 1 E, F), only a minority of UBAP2L and G3BP particles colocalized
141 (Pearson Coefficient: 0.03 ± 0.19, mean ± SD).

142 These results demonstrate that stress granules contain at least two distinct populations of
143 UBAP2L (a mobile fraction and an immobile one) and that UBAP2L localizes in discrete

144 particles reminiscent of stress granule cores. However, UBAP2L particles and G3BP1 cores

145 do not colocalize, suggesting that UBAP2L particles are distinct from G3BP1 stress granule

146 cores.

147

148 **UBAP2L is essential for stress granule assembly induced by many cellular stressors.**

149 G3BP1 forms particles inside stress granules (Jain et al., 2016) and is an important regulator

150 of stress granule formation (Kedersha et al., 2016). Our data demonstrate that UBAP2L also

151 exists in particles, suggesting it may play an important role in stress granule assembly, like

152 G3BP1.

153 Since stress granules induced by different stressors show different compositions (Fujimura

154 et al., 2012; Kedersha et al., 2008), we asked whether UBAP2L is a general stress granule

155 component or whether it displays a stress-specific recruitment. We exposed HeLa K cells to

156 a variety of stresses (see Material and Methods) and stained them with anti-G3BP

157 antibodies as a marker for stress granules and with anti-UBAP2L antibodies. We imaged

158 the cells with confocal microscopy and evaluated the Pearson colocalization coefficient of

159 UBAP2L with G3BP1 (Fig. 2A, B). We found that UBAP2L formed granules that colocalized

160 with G3BP1 stress granules in arsenite treatment, endoplasmic reticulum (ER) stress (DTT),

161 proteasome inhibition (MG132), heat shock and mitochondrial stress (NaN$_3$, Fig 2 A, B). The

162 colocalization score was low after the 90° rotation in the cytoplasm of non-treated control

163 cells and in arsenite-treated cells, excluding the possibility of a random colocalization

164 between the two fluorescent signals (Fig. S2A, B).These results show that UBAP2L is a

165 general component of stress granules, consistent with recent data (Huang et al., 2019).

166 UBAP2L is required for stress granule assembly in cells stressed with arsenite, H$_2$O$_2$ and

167 Sorbitol (Huang et al., 2019; Markmiller et al., 2018; Youn et al., 2018). We next tested

168 whether UBAP2L was also required for stress granule assembly in the conditions that we

169 tested above (ER stress, proteasome inhibition, heat shock and mitochondrial stress). We

170 depleted UBAP2L using two independent siRNAs and found that both siRNAs strongly

171 reduce UBAP2L signal (97.0 ± 1.9 % depletion for siUBAP2L #1, 97.6 ± 1.7 % depletion for

172 siUBAP2L #2, mean ± SEM) when compared to cells transfected with a control siRNA (Fig.

173 S2 C, D). We then visualized stress granules with anti-G3BP antibodies in cells exposed to

174 ER and mitochondrial stress, proteasome inhibition and heat shock in the absence of

175 UBAP2L. In control-depleted cells, stress granules promptly assembled following stress,

176 whereas non-treated cells rarely assembled stress granules (Fig. 2 C, D). Different

177 treatments result in the formation of stress granules of different size and shape (Fig. 2 C),

178 as previously described (reviewed in Mahboubi and Stochaj, 2017; Panas et al., 2016;

179 Protter and Parker, 2016). Compared to control depleted cells, UBAP2L depletion cause a

180 significant reduction of the percentage of cells displaying G3BP1-positive stress granules

181 (Fig. 2 C, D). We observed the same requirement for UBAP2L in arsenite-induced stress

182 granule formation when using antibodies against TIA-1 or USP10 as alternative stress

183 granule markers, excluding that the role of UBAP2L is limited to G3BP1 (Fig. S2 E).

184 These results show that UBAP2L is a general component of stress granules and it is not

185 only required for arsenite-induced stress granule assembly (Markmiller et al., 2018; Youn et

186 al., 2018) but also for stress granules assembly in other stress conditions, consistent with

187 recent data (Huang et al., 2019). It is interesting that UBAP2L is required for stress granule

188 assembly in heat-shock conditions. G3BP1 is not required for heat-induced stress granule

189 formation (Kedersha et al., 2016), suggesting that UBAP2L plays a more general role than

190 G3BP1.

191

192 **UBAP2L promotes stress granule assembly upstream of G3BP1.**

193 Stress granules cannot form in absence of the proteins G3BP1 and G3BP2 (Kedersha et

194 al., 2016; Matsuki et al., 2013). To test whether UBAP2L requires G3BP1 and 2 for its

195 localization to stress granules, we co-depleted both G3BP1 and 2 in HeLa K cells (Fig. S3).

196 Following UBAP2L depletion, we induced stress granule formation using arsenite and then

197 fixed and stained cells with anti-UBAP2L and anti-G3BP antibodies (Fig 3 A). Compared to

198 control-depleted cells, the percentage of cells containing UBAP2L positive granules did not

199 significantly change when G3BP1 and 2 were depleted (Fig. 3 B), suggesting that G3BP1

200 and 2 are dispensable for stress granules recruitment of UBAP2L.

201 Because of the pitfalls of transient protein depletion, we cannot formally exclude that a small

202 pool of G3BP1 and 2 is sufficient for the formation of UBAP2L positive stress granules. To

203 tackle this problem, we used G3BP1 and 2 knock-out U2OS cells (Fig. 3 C, Kedersha et al.,

204 2016). Immunofluorescence analysis of these cells after arsenite treatment revealed that

205 UBAP2L localizes into cytosolic granules (Fig 3 C, D), confirming that UBAP2L granule

206 formation is independent of G3BP1 and 2. In both HeLa K and U2OS cell lines the depletion

207 or the knock-out of G3BP1 and 2 result in a reduction of stress granule size compared to

208 control cells (Fig. E, F) indicating that G3BP1 and 2 are important for stress granule

209 maturation.

210 Our results support a model in which UBAP2L acts upstream of other stress granule

211 nucleators such as G3BP1 and 2.

8

212

213

Inhibition of translation after stress does not depend on UBAP2L.

Since our results show that UBAP2L is necessary for stress granule assembly in several conditions and acts upstream of G3BP1, we reasoned that the absence of UBAP2L may affect the signaling pathway upstream of stress granule nucleation. Stress granule assembly is a multistep process that requires inhibition of translation and polysome disassembly (reviewed in Mahboubi and Stochaj, 2017; Panas et al., 2016; Protter and Parker, 2016). An early step in arsenite-induced stress granule assembly is the phosphorylation of the elongation factor eIF2α (Eukaryotic Initiation Factor 2 α) on Serine 51. To assess whether UBAP2L contributes to eIF2α phosphorylation in stress conditions, we depleted UBAP2L and exposed the cells to arsenite. Western blot using an antibody directed against pS51-eIF2α revealed no difference between cell lysates depleted for UBAP2L and control (Fig. 4 A), indicating that UBAP2L it is not required for eIF2α phosphorylation after stress.

Next, we asked whether cells depleted for UBAP2L efficiently inhibit translation after stress. To answer this question, we used a puromycilation assay; as puromycin covalently binds to nascent peptides, puromycin incorporation can be used as a readout for the rate of translation (Azzam and Algranati, 1973; Goodman et al., 2012; Schmidt et al., 2009). Western blot analysis with an anti-puromycin antibody revealed that arsenite treatment strongly reduces puromycin incorporation in both control and UBAP2L depleted cells (Fig. 4 B), indicating that UBAP2L is not required for arsenite induced translation inhibition.

Following translation inhibition, a crucial step in stress granule formation is the disassembly of polysomes. Drug treatments stabilizing polysomes, such as cycloheximide, inhibit stress granule formation (Bounedjah et al., 2014; Buchan et al., 2011; Kedersha et al., 2000; Mokas et al., 2009). Since we did not detect a role of UBAP2L in arsenite induced translation inhibition, we investigated the requirement of UBAP2L in polysome disassembly. To this end, we developed an assay to follow polysome disassembly in live cell imaging, using a previously published polysome reporter cell line (Pichon et al., 2016). Following siRNAs transfection, HeLa cells containing a fluorescent polysome reporter were treated with arsenite and imaged for 30 minutes. Counting the number of polysomes over time, we found that polysomes disappeared ≈15 minutes after the addition of stress in control depleted cells (Fig. 4 C). As a positive control, we compared arsenite-treated cells with cells treated with both arsenite and cycloheximide (CHX). Cells receiving this double treatment displayed only a modest rate of polysome decay, compared with cells receiving arsenite alone, indicating

9

246　that our assay efficiently detects a polysome disassembly defect *in vivo* (Fig. 4 C). Similar

247　to control depleted cells, UBAP2L depletion did not prevent arsenite-induced polysome

248　disassembly (p=0.4692 for siUBAP2L #1 and p=0.4544 for siUBAP2L #2, two-way ANOVA

249　and Dunnett's multiple comparison). This result suggests that UBAP2L is not required for

250　polysome disassembly following an arsenite treatment.

251　An early event in stress granule formation is the coalescence of PICs in stress granule cores

252　(reviewed in Panas et al., 2016). UBAP2L could potentially act upstream of this process,

253　constituting the first stress granule seed. To test this hypothesis, we stressed HeLa cells

254　with arsenite alone or a combination of arsenite and cycloheximide. We then fixed and

255　stained the cells with anti-UBAP2L and anti-G3BP antibodies. Following arsenite treatment,

256　both UBAP2L and G3BP1 coalesce into stress granules (Fig. 4 D, Markmiller et al., 2018;

257　Youn et al., 2018), whereas treatment with arsenite and cycloheximide together prevented

258　the formation of both UBAP2L and G3BP1 positive stress granules (Fig. 4 D, E). This result

259　shows that UBAP2L cannot nucleate stress granules before polysome disassembly and

260　polysome-derived PIC formation.

261　These data together show that UBAP2L recruitment to stress granules depends on

262　polysome derived PICs but it is independent of other stress granule nucleators.

263

264   DISCUSSION

265   The inner structure of stress granules and several aspects of the pathway leading to stress

266   granule formation remain controversial. Here, we investigated the stress granule protein

267   UBAP2L and found that it behaves as a stress granule core component, yet it does not

268   colocalize with G3BP1 cores. We showed that recruitment of UBAP2L to stress granules

269   requires polysome disassembly but is independent of G3BP1, suggesting that UBAP2L

270   coalescence precedes G3BP1 recruitment to stress granules.

271   Our data are not contradictory with the proposed function of G3BP1 and 2 as essential stress

272   granule nucleators (Kedersha et al., 2016; Matsuki et al., 2013). Albeit G3BP1 and 2 are not

273   required for the formation of UBAP2L positive stress granules, they are important to recruit

274   other components and to form a mature stress granule (Kedersha et al., 2016; Matsuki et

275   al., 2013). In agreement, we observed a decrease in UBAP2L granule size after G3BP1 and

276   2 depletion (Fig. 3 E, F). The absence of both G3BP1 and 2 results in UBAP2L positive

277   stress granule of similar size in HeLa K (0.196 ± 0.100 μm^2) and U2OS cells (0.283 ± 0.169

278   μm^2; Mean ± SD), suggesting that stress granule may have a lower size limit. These

279   measurements are too close to the diffraction limit of our experiment to be conclusive.

280   Nevertheless, one can speculate that in absence of G3BP1 and 2, only isolated UBAP2L

281   cores assemble, suggesting that, in normal conditions, UBAP2L cores come first in stress

282   granules nucleation, whereas G3BP1 cores are required later for stress granules maturation

283   (Fig. 4 F). The upstream role of UBAP2L is also consistent with recent work showing that

284   depletion of UBAP2L results in the loss of the interaction of G3BP2 with ribosomal subunits

285   (Huang et al., 2019).

286   Altogether, our results provide evidence that core particles of different nature coexist in the

287   same stress granule. We propose a model in which both G3BP1 and UBAP2L bind stalled

288   preinitiation complexes, but they contribute differently to stress granule assembly (Fig. 4 F).

289   UBAP2L acts upstream of G3BP1, preceding the formation and/or the recruitment of G3BP1

290   cores inside the stress granules. An intriguing possibility is that UBAP2L and G3BP1

291   particles reflect distinct pools of preinitiation complexes, possibly linked to different mRNA

292   species. Further work is needed to test these hypotheses and develop a comprehensive

293   model of stress granule nucleation. Other stress granule components, such as PABP1 and

294   mRNAs, form a core-like pattern inside stress granules suggesting that even more core

295   species exist (Jain et al., 2016; Souquere et al., 2009; Wheeler et al., 2016).

296   The role of UBAP2L in stress granule nucleation is of interest from a clinical perspective.

297   Several stress granule proteins contribute to neurodegenerative disorders such as

11

298 Amyotrophic Lateral Sclerosis (ALS) or Frontal Temporal Lobar Dementia (FTLD) (Jain et
299 al., 2016; Markmiller et al., 2018; Youn et al., 2018; reviewed in Li et al., 2013; Ramaswami
300 et al., 2013). For example, stress granule independent phase separation of TDP-43 (TAR)
301 DNA binding protein), a hallmark of ALS, causes cell death in neurons (Gasset-Rosa et al.,
302 2019), suggesting that a functional stress granule machinery has a protective effect towards
303 neurodegeneration. In *D. melanogaster*, modulating the levels of the proposed ortholog of
304 UBAP2L, Lingerer, has an influence on FUS and FTD/ALS-associated poly(GR) protein
305 toxicity (Markmiller et al., 2018).

306 Aside from neurodegeneration, a number of publications show a role of UBAP2L in cancer.
307 UBAP2L appears to act in different malignances as an oncogene, whose expression is
308 required for survival (Chai et al., 2016), growth (He et al., 2018; Li and Huang, 2014; Li et
309 al., 2018; Zhao et al., 2015), and metastasization (Aucagne et al., 2017; Li and Huang, 2014;
310 Li et al., 2018; Ye et al., 2017). Stress granules are often present in cancer cells (reviewed
311 in Mahboubi and Stochaj, 2017), where they may promote cell survival in the stressful
312 condition of the cancer microenvironment (Adjibade et al., 2015; Somasekharan et al., 2015;
313 Vilas-Boas et al., 2016) and metastasization (Somasekharan et al., 2015). Interfering with
314 stress granule formation by reducing G3BP1 expression, has a protective effect towards
315 metastasization in mice (Somasekharan et al., 2015). In analogy with G3BP1, inhibiting
316 stress granule formation in cancer cells by targeting UBAP2L represents a therapeutic
317 option that is worth further investigation.

318 In conclusion, our results show that UBAP2L is a core component of stress granules and is
319 a crucial regulator of stress granule assembly in many stress conditions. UBAP2L may
320 therefore represent an attractive therapeutic target for the treatment of neurodegenerative
321 diseases and cancer.

322
323
324
325
326
327
328
329
330
331
332

333   STAR METHODS

334   **Key Resource Table**

335   Table S1

336

337   **Contact for Reagent and Resource Sharing**

338   Further information and requests for resources and reagents should be directed to and will

339   be fulfilled by the Lead Contact, Monica Gotta (monica.gotta@unige.ch)

340

341   **Experimental Model and Subject Details**

342   HeLa Kyoto (HeLa K) and U2OS cells were grown in DMEM (Gibco) supplemented with

343   10% fetal calf serum (FCS; Gibco), 2 mM L-glutamine, 100 U/ml penicillin, and 100 µg/ml

344   streptomycin (Invitrogen). Cells were maintained in an humidified incubator at 37°C and 5%

345   CO_2 concentration. For live cell imaging experiment and heat shock treatment (Fig. 1 C, S1

346   F, Fig. 2, Fig. 4 C) cells were imaged in Leibovitz L-15 (Thermofisher) medium supplemented

347   with 10% FCS.

348

349   METHOD DETAILS

350   **Cell transfection and treatments**

351   For STED (Fig. 1 A, B, E, F and Fig S1 A), 300'000 cells were seeded on 20 mm high

352   precision coverslips (Karl Hecht) in a 6 well plate/35 mm dish, 24 hours before the

353   experiment. For experiments in Fig. 1 G, H, I and Fig. 2 and Fig. 3 cells were seeded 30-

354   40% confluent on a 1 cm round coverslip, 24 hours prior to transfection. For experiments in

355   Fig. 4 A, B, Fig. S1 D, E and Fig S3, 150'000 HeLa K cells were seeded in a 6 well plate/35

356   mm dishes, 24 hours prior to transfection. In Fig. 3C, 5000 PolII-SunTagx56-Ki67-MS2x132

357   HeLa cells (Pichon et al., 2016), were seeded in a 8-well IBIDI plate (Vitaris). For

358   experiments in Fig. 4 D, E 100'000 cells were seeded on 20 mm square coverslips in a 6

359   well plate/35 mm dishes, 24 hours prior to transfection.

360   Transfection was performed with a final concentration of 20 nM siRNAs and carried out using

361   LipofectamineTM RNAiMAX transfection Reagent according to the manufacturer's

362   instructions (Invitrogen). The following target sequences were used (Dharmacon):

363   • 5'-GCAAUAGCAGCGGCAAUACGUdTdT-3' (siUBAP2L #1),

364   • 5'-CAACACAGCAGCACGUUAUdTdT-3' (siUBAP2L #2),

365   • 5'- CUUACAACGUCGACCGCAAdTdT-3' (simScarlet),

366   • 5'- ACAUUUAGAGGAGCCUGUUGCUGAAdTdT -3'(siG3BP1),

13

367   •   5'- GAAUAAAGCUCCGGAAUAUdTdT-3' (siG3BP2),

368   •   5'- GGACCUGGAGGUCUGCUGUdTdT-3'(siCTR).

369 In codepletion experiments (Fig. 3 A, B, E) a total of 40 nM siRNA was used: in the single

370 depletions 20 nM siG3BP1 or 2 were mixed with 20 nM siCTR to account for siRNA

371 competition. In all the experiments a 48-hours siRNA treatment was performed.

372 For ER stress (Fig. 2), HeLa K were treated with 2 mM Dithiothreitol (DTT, Sigma) diluted

373 into culture medium for 30 minutes at 37°C. For Proteasome Inhibition (Fig. 2), HeLa K were

374 treated with 10 µM MG132 (Sigma) diluted into culture medium at 37°C. For heat shock (Fig.

375 2), HeLa K were transferred to L-15 medium and incubated for 3 hours at 37°C, then the

376 temperature was increased at 42°C for 60 minutes. For mitochondrial stress (Fig. 2), HeLa

377 K were treated with 75 mM NaN$_3$ (Sigma) for 30 minutes at 37°C. Regarding arsenite stress

378 cells were treated with 0.1-0.5 mM Sodium Arsenite (Sigma) for 30-60 minutes, the exact

379 conditions are indicated for each figure in the corresponding figure legend.

380 Cycloheximide (Merk) was diluted in culture medium at a final concentration of 50 µg/ml.

381 Puromycin (Sigma) was diluted in culture medium at a final concentration of 10 µg/ml.

382

383 **Creation of HeLa-UBAP2LmScarlet CRISPR cell line**

384 HeLa K were transfected using xtremeGene9 (Sigma) with 500 ng of an all-in-one plasmid

385 (Sigma) expressing Cas9-eGFP and the sgRNA 5'- ACAGCTGGGGGGGCCAACTG -3'

386 (targeting UBAP2L). The all-in-one plasmids were cotransfected with 500 ng of pUC57

387 plasmid containing a repair template (Genewiz). The repair template was designed as a

388 fusion of 5xGly-mScarlet flanked by two 500 bp arms, homologous to the genomic region

389 around the Cas9 cutting site. 5 days after transfection, 3000 mScarlet positive cells were

390 sorted in a 1 cm well and expanded for one week before a second sorting of single cells in

391 a 96 well plates. Single colonies were grown in conditioned medium (50% fresh culturing

392 medium and 50% filtered medium harvested from a confluent culture of HeLa K cells

393 after 24 hours). Sorting was performed using an astrios MoFlo Cell Sorter (Beckman). After

394 2-3 weeks cells were screened by PCR. Briefly, cells were split and part of the cells from

395 each clone were lysed and the DNA extracted using a commercial kit according to the

396 manufacturer's instructions (Quiagen). The genomic DNA obtained was subjected to PCR.

397 Positive clones were identified according to the size of the PCR product and further

398 screened by Western Blot. PCR amplification was performed using Taq Polymerase (Roche)

399 according to manufacturer instruction. PCR products were separated through

400 electrophoresis in a TBE (89 mM Tris-borate, 2mM EDTA in ddH$_2$O pH 8.3) 1% Agarose gel

401   for 20 minutes at 100 V in TBE buffer. Then the agarose gel was stained with 0.2-0.5 µg/ml

402   Ethidium bromide in ddH$_2$O for five minutes and the PCR products were visualized using an

403   UV transilluminator (Syngene).

404

Antibodies

406   The following antibodies were used: Mouse anti-eIF2α (1:1000 Cell Signalling L57A5),

407   Mouse anti-G3BP (1:1000 – 1 µg/ml BD Biosciences 611126), Rabbit anti-G3BP2 (1:1000

408   Bethyl A302-040A) Rabbit anti-PCNA (1:1000 – 1 µg/ml Abcam ab18197), Rabbit anti-pS51-

409   eIF2α (1:500 – 0.721 µg/ml ab32157), Mouse anti-Puromycin (1:25000 Sigma-Aldrich

410   MABE343 [12D10]), Rabbit anti-TIA1 (1:1000 – 5 µg/ml Abcam ab40693), Mouse anti-

411   αTubulin (1:1000 Sigma-Aldrich T9026), Rabbit anti-UBAP2L (1:2000 – 1 µg/ml Abcam

412   ab138309), Rabbit anti-USP10 (1:200 – 1 µg/ml Abcam ab70895), AlexaFluor donkey anti-

413   mouse 488nm (1:400 – 0.5 µg/ml Thermo Fisher A21202), AlexaFluor donkey anti-rabbit

414   488nm (1:400 – 4 µg/ml Thermo Fisher A11034), AlexaFluor goat anti-rabbit 594nm

415   (1:400 – 2 µg/ml Thermo Fisher A11012), HRP-conjugated goat anti–mouse (1:10000

416   BioRad 170-6516), HRP-conjugated goat anti–rabbit (1:10000 BioRad 170-6515).

417   For U-ExM both the primary and the secondary antibody concentrations were doubled. For

418   STED the following secondary antibodies were used: Goat anti-mouse STAR RED (1:5000

419   Abberior STRED), Goat anti-mouse STAR RED (1:5000 Abberior STRED), AlexaFluor

420   donkey anti-rabbit 488nm (1:5000 – 0.2 µg/ml Thermo Fisher A11034).

421

Immunofluorescence

423   HeLa K cells were seeded on HCl-treated coverslips and fixed with 4% formaldehyde (FA,

424   Sigma) in Phosphate Saline Buffer (PBS, 137 mM NaCl, 2.7 mM KCl, 10 mM Na$_2$HPO$_4$, 1.8

425   mM KH$_2$PO$_4$ in ddH$_2$O) for 10 min at room temperature (RT). Cells were permeabilized for

426   10 minutes with PBS-0.1% Triton X-100 (Sigma-Aldrich). For STED cells were

427   permeabilized with PBS-0.1% Tween-20 (Sigma-Aldrich). Cells were incubated in blocking

428   buffer (1% Bovine Serum Albumin (BSA - Sigma-Aldrich), 0.02 % NaN$_3$, PBS) for 1 hr at RT

429   and then incubated for an additional hour with primary antibodies diluted in blocking buffer.

430   Coverslips were then washed in PBS-0.1% Tween-20 and incubated for 1 hour at RT with

431   secondary antibodies diluted in blocking buffer and 1 mg/mL 4'6'-Diamidino-2-phenylindole

432   (DAPI) (Sigma Aldrich). Coverslips were there mounted with either Vectashield with DAPI

433   mounting medium (ReactoLab) or with Mowiol (Sigma Aldrich). For STED no DAPI

434   counterstaining was performed and the samples received an additional washing step with

15

435 tap water prior to mounting. The samples were mounted using ProLong™ Gold Antifade

436 Medium (Thermofisher).

437 Images in Fig. 2, 3, 4 and Fig S 2 were obtained with an A1r spectral confocal microscope

438 (Nikon) equipped with a 60× 1.4 NA CFI Plan Apochromat Lambda oil objective and 4 PMTS

439 including 2 GaAsp for detection. Except for Fig. 1, Fig. 2 B and Fig S2 B, all the

440 quantifications were obtained imaging the cells with either a Leica DM6000 microscope

441 (Leica Microsystems) equipped with epifluorescence and DIC optics, 63×/1.4 numerical

442 aperture (NA) objective, and a DFC 360 FX camera (Leica), or a Nikon microscope (Nikon)

443 equipped with epifluorescence and DIC optics, 63×/1.4 numerical aperture (NA) objective,

444 camera.

445

446 **Live Cell Imaging**

447 Image series displayed in Fig. S1 F and Fig. 3 C were obtained recording cells growing in

448 IBIDI plates at 37°C using a Nikon Eclipse Ti-E wide-field microscope (Nikon, Switzerland)

449 equipped with a DAPI/eGFP/TRITC/Cy5 filter set (Chroma, USA), a 60× NA 1.3 oil-objective

450 (Fig. S1 F) or a 100× NA 1.4 oil-objective (Fig. 4 C) and a Orca Flash 4.0 CMOS camera

451 (Hamamatsu, Japan) and the NIS software. In Fig. S1 F, 11 Z-stacks (Step size = 1 μm)

452 were taken every 60 seconds, for 30 minutes, using 5 % lamp power and recording 576 nm

453 emission for 200 ms Exposure, with 2x2 Binning. In Fig. 4 C, 15 Z-stacks (Step size = 0.6

454 μm) were taken every 30 seconds, for 30 minutes, using 3% lamp power and recording 535

455 nm emission for 200 ms Exposure, with 2x2 Binning.

456 For FRAP experiment (Fig. 1 C, D and Fig S1 G, H) single plane images of HeLa UBAP2L-

457 mScarlet were acquired at 37°C every 2 seconds using an A1r spectral confocal microscope

458 (Nikon) equipped with a 60× 1.4 NA CFI Plan Apochromat Lambda oil objective and 4 PMTS

459 including 2 GaAsp for detection. Imaging was performed with 2X line averaging and 0.260

460 μm pixel size. Photobleaching was performed with 100% 561 nm laser on a ≈2 μm diameter

461 area (Scan Speed = 0.25). A single stress granule was followed for 10 seconds, bleached,

462 recorded for 3 minutes (Fist FRAP cycle), bleached a second time and recorded for 3

463 minutes (Second FRAP Cycle). NIS Elements AR software (v.4.20.01; Nikon) was used to

464 set acquisition parameters.

465

466 **STED super-resolution microscopy**

467 For STED we used a pulsed gated-STED microscope DMi8 equipped with HC PL Apo 93x/

468 1.30 glycerol motC STED W objective and a DFC7000T camera (Leica). Excitation was

469 performed with a white laser, whereas depletion with either a continuous 592 nm laser or a

470 775 nm pulsed laser.

471 For 3D-STED imaging (Fig 1 A), stress granules were imaged in 3D using a 7% 635 nm

472 laser and depletion was performed with 15% 775 nm laser, with 15% laser power in 3D

473 STED. Imaging was performed with 4X line averaging and ≈20 nm pixel size. 3D stacks

474 were acquired with a step size of 100 nm. For 2D-STED dual color (Fig. 1 E) stress granules

475 were imaged in 2D using a 7% 635 nm excitation laser + 15% 775 nm depletion laser,

476 followed by a 10% 488 nm excitation laser + 15% 592 nm depletion laser. Imaging was

477 performed with 4X line averaging and ≈20 nm pixel size. Images were deconvolved using

478 Huygens (Scientific Volume Imaging).

479

480 **Ultrastructure Expansion Microscopy (U-ExM)**

481 U-ExM was performed as described in (Gambarotto et al., 2019). Briefly, in Fig. 1 G, H, I the

482 cells were grown in 12 mm slides and then fixed with 4% FA (Sigma) in PBS for 10 min at

483 37°C. Then, coverslips were incubated in a solution of 0.7% FA, 1% AA (Acrylamide, Sigma)

484 in PBS for 5 h at 37 °C. Gelation was performed in a precooled humid chamber with

485 coverslips facing up with 35 µl of monomer solution (19% Sodium Acrylate (SA, Sigma),

486 10% AA, 0.1% BIS (N,N'-methylenbisacrylamide, Sigma) in PBS supplemented with

487 0.5% APS and 0.5% TEMED. Immediately after the addition of MS the chamber was closed

488 with a second coverslip on top. Coverslips were then incubated for 1 hour at 37 °C in the

489 dark. Coverslips with gels were transferred into 2 ml of denaturation buffer (200 mM SDS

490 (Sodium dodecyl sulfate, Sigma), 200 mM NaCl (Sigma), and 50 mM Tris (Biosolve) in

491 ddH$_2$O, pH 9) for 15 min at RT. Samples were then placed into a 1.5-ml Eppendorfs filled

492 with fresh denaturation buffer, and incubated at 95 °C for 1 hour. After denaturation, gels

493 were expanded in beakers filled with ddH$_2$O. Water was exchanged three times every 30 min

494 at RT, for the last wash samples were incubated O/N in ddH$_2$O at 4°C. Next, gels were

495 placed in PBS two times for 15 min. Primary antibodies were diluted in 2% BSA PBS and

496 binding was performed at 37 °C for 3 h. Gels were then washed in 0.1% Tween 20 PBS

497 three times for 10 min at RT. The same steps were repeated for secondary antibodies.

498 Finally, gels were placed in ddH$_2$O. Water was exchanged three times every 30 min, and

499 then gels were incubated in ddH$_2$O overnight.

500 For imaging, a piece of gel was mounted in a 2-well IBIDI plate coated with poly-L-lysine

501 (Sigma). Confocal microscopy was performed using an A1r spectral confocal microscope

502 (Nikon) equipped with a 60× 1.4 NA CFI Plan Apochromat Lambda oil objective and 4 PMTS

17

503 including 2 GaAsp for detection. 3D z-stacks at 100 nm steps were acquired with a pixel

504 size of 50 nm. Images were deconvolved using Huygens.

505

Western Blotting

507 HeLa extracts were prepared from HeLa K or HeLa UBAP2L-mScarlet cells by scraping the

508 cells in 50 mM Tris-HCl (pH 7.4), 150 mM NaCl, 1 mM EDTA, 1 mM EGTA, 0.27 M sucrose,

509 1% Triton X-100, complete protease inhibitor cocktails (Roche), and phosphatase inhibitor

510 PhosSTOP (Roche) for 1 hour on ice before clarification by centrifugation (14'000 g 20

511 minutes, 4°C). Supernatants were collected and quantified using Bradford Reagent (Bio-

512 Rad Laboratories). Lysates were then diluted in Laemmli buffer and a 30 µg of lysates were

513 separated by SDS-PAGE using a manually poured 10% Acrylamide Gel. Proteins were then

514 transferred onto a nitrocellulose membrane (Sigma). The membrane was blocked with 5%

515 BSA in TBS (Tris-Buffered Saline, 50 mM Tris-Cl, 150 mM NaCl, in ddH$_2$O, pH 7.4) and

516 incubated overnight with primary antibodies at 4°C in the same solution. The following day

517 the membrane was washed with 0,1% Tween TBS and incubated with secondary antibodies

518 in 0,1% Tween TBS. Proteins were visualized with ECL (Millipore).

519 Western blot quantification (Fig S2 C) was performed calculating the area under the curve

520 using Fiji's "Gel" plugin. UBAP2L quantification was normalized on the corresponding tubulin

521 signal and then on the average UBAP2L levels in control depleted cells of 4 independent

522 experiments. Resulting values were scaled from 0 to 100. Statistical analysis was performed

523 with Prism 8 (GraphPad).

524

Particle Diameter Measurement, Line Profiles and stress granule areas

526 In Fig. 1 B and Fig. S1 A particle diameters was measured using Imaris 9.2 (Bitplane) and

527 data were analyzed with Python 3.7.0 and the libraries "pandas", "matplotlib.pyplot" and

528 "numpy". Particles below 0.06 µm were excluded from the analysis (8.75 % of the G3BP1

529 particles, 4.87 % of the UBAP2L particles). n= 857 particles (44 stress granules, 38 cells)

530 for G3BP, n= 904 particles (84 stress granules, 67 cells) for UBAP2L.

531 In Fig. 1 F, I line profiles were calculated for both channels drawing a line on a stress granule

532 and using FiJi "Plot Profile" function. The pixel by pixel gray value was normalized on the

533 average grey value of all pixels in the line. Data were analyzed with Prism 8. In Fig. 1 G the

534 3D surface of the stress granules particles was computed using Imaris 9.2.

535 To quantify stress granule areas in Fig. 3 E, F we created a Image J macro available on

536 github: https://github.com/LCirillo/FiJiMacro/blob/master/IJ_Macro_SG_Area. For each

537   independent experiment a minimum of 53 stress granules and were measured for each

538   condition.

539

540   **FRAP quantification**

541   In Fig. 1D and Fig. S1 G, H, the bleached stress granule was tracked using Imaris 9.2 and

542   the mean grey intensity over time was measured (FI). In parallel, the total fluorescence of

543   the image (FI$_{tot}$). After background subtraction the data were normalized as follows to

544   account for photobleaching and fluorophores loss:

545

546
$$Value(t) = \left. \frac{FI_{(t)}}{FI_{(pre)}} \middle/ \frac{FI_t^{tot}}{FI_{pre}^{tot}} \right.$$

547   All the particles that did not recover to 1 in the second FRAP were excluded from the final

548   analysis (32.5 %). Data analysis was carried out using Prism 8. Result were averaged

549   separately for the 1st FRAP and the 2nd FRAP and plotted as mean +/- 95% CI. The mean

550   recovery curve was fitted to a single exponential using Fiji (FRAP1 R2= 0.985, FRAP2

551   R2=0.988) and the immobile fraction extrapolated. Statistical analysis was performed with

552   Prism 8.

553

554   **Colocalization analysis**

555   In 2D STED and Expansion microscopy (Fig. 1 E, H) Pearson's Correlation Coefficient was

556   measured using Imaris 9.2. n= 20 stress granules from 11 cells (2D STED), n=28 stress

557   granules from 7 cells (U-ExM).

558   For the cross-correlation analysis of the distributions of UBAP2L and G3BP1 (Fig. 2 B, Fig.

559   S2 B) the Pearson's Correlation Coefficient was measured using single plane confocal

560   images of HeLa K cells experiencing different stresses. The Pearson Coefficient was

561   measured using the Fiji plugin "Coloc2". Cololcalization analysis was performed as

562   previously described (Martino et al., 2017). Statistical analysis was performed using Prism

563   8.

564

565   **Polysome Decay Assay**

566   To segment and quantify polysome decay in Fig. 4 C we created an Image J macro available

567   on github: https://github.com/LCirillo/FiJiMacro/blob/master/IJ_Macro_PolysomeCounting.

568   The number of polysomes obtained was divided by the surface occupied by the cells to
569   obtain the polysome density (PD). The polysome density at each time point (Pd_t) was
570   normalized by the polysome density at the first frame of imaging (Pd_0) to obtain the
571   normalized polysome density.

572
$$Normalized\ Polysome\ Density = \frac{Pd_t}{Pd_0}$$

573   Data analysis was carried out using Prism 8.

574

575   **Figure assembly**

576   All the figures were assembled using Adobe Illustrator CS6.

577

578

579

580

581

582

583

584

585

ACKNOWLEDGMENTS

AUTHOR CONTRIBUTIONS

A.C. and L.C. performed all the experiments, quantifications and interpreted the results. L.C. and M.G wrote the manuscript and conceived the study. M.G. acquired funding.

DECLARATION OF INTEREST

The authors declare no competing interests.

604 REFERENCES

605 Adjibade, P., St-Sauveur, V.G., Huberdeau, M.Q., Fournier, M.-J., Savard, A., Coudert, L.,
606   Khandjian, E.W., Mazroui, R., 2015. Sorafenib, a multikinase inhibitor, induces
607   formation of stress granules in hepatocarcinoma cells. Oncotarget 6, 43927–43943.
608 Aucagne, R., Girard, S., Mayotte, N., Lehnertz, B., Lopes-Paciencia, S., Gendron, P.,
609   Boucher, G., Chagraoui, J., Sauvageau, G., 2017. UBAP2L is amplified in a large
610   subset of human lung adenocarcinoma and is critical for epithelial lung cell identity
611   and tumor metastasis. FASEB J. 31, 5012–5018.
612   https://doi.org/10.1096/fj.201601219RRR
613 Aulas, A., Vande Velde, C., 2015. Alterations in stress granule dynamics driven by TDP-43
614   and FUS: a link to pathological inclusions in ALS? Front Cell Neurosci 9.
615   https://doi.org/10.3389/fncel.2015.00423
616 Azzam, M.E., Algranati, I.D., 1973. Mechanism of puromycin action: fate of ribosomes
617   after release of nascent protein chains from polysomes. Proc. Natl. Acad. Sci.
618   U.S.A. 70, 3866–3869.
619 Beck, M., Schmidt, A., Malmstroem, J., Claassen, M., Ori, A., Szymborska, A., Herzog, F.,
620   Rinner, O., Ellenberg, J., Aebersold, R., 2011. The quantitative proteome of a
621   human cell line. Mol Syst Biol 7, 549. https://doi.org/10.1038/msb.2011.82
622 Bindels, D.S., Haarbosch, L., van Weeren, L., Postma, M., Wiese, K.E., Mastop, M.,
623   Aumonier, S., Gotthard, G., Royant, A., Hink, M.A., Gadella, T.W.J., 2017.
624   mScarlet: a bright monomeric red fluorescent protein for cellular imaging. Nat.
625   Methods 14, 53–56. https://doi.org/10.1038/nmeth.4074
626 Bounedjah, O., Desforges, B., Wu, T.-D., Pioche-Durieu, C., Marco, S., Hamon, L., Curmi,
627   P.A., Guerquin-Kern, J.-L., Piétrement, O., Pastré, D., 2014. Free mRNA in excess
628   upon polysome dissociation is a scaffold for protein multimerization to form stress
629   granules. Nucleic Acids Res. 42, 8678–8691. https://doi.org/10.1093/nar/gku582
630 Buchan, J.R., Yoon, J.-H., Parker, R., 2011. Stress-specific composition, assembly and
631   kinetics of stress granules in Saccharomyces cerevisiae. J. Cell. Sci. 124, 228–239.
632   https://doi.org/10.1242/jcs.078444
633 Chai, R., Yu, X., Tu, S., Zheng, B., 2016. Depletion of UBA protein 2-like protein inhibits
634   growth and induces apoptosis of human colorectal carcinoma cells. Tumour Biol.
635   37, 13225–13235. https://doi.org/10.1007/s13277-016-5159-y
636 Fujimura, K., Sasaki, A.T., Anderson, P., 2012. Selenite targets eIF4E-binding protein-1 to
637   inhibit translation initiation and induce the assembly of non-canonical stress
638   granules. Nucleic Acids Res. 40, 8099–8110. https://doi.org/10.1093/nar/gks566
639 Gambarotto, D., Zwettler, F.U., Le Guennec, M., Schmidt-Cernohorska, M., Fortun, D.,
640   Borgers, S., Heine, J., Schloetel, J.-G., Reuss, M., Unser, M., Boyden, E.S., Sauer,
641   M., Hamel, V., Guichard, P., 2019. Imaging cellular ultrastructures using expansion
642   microscopy (U-ExM). Nat. Methods 16, 71–74. https://doi.org/10.1038/s41592-018-
643   0238-1
644 Gasset-Rosa, F., Lu, S., Yu, H., Chen, C., Melamed, Z., Guo, L., Shorter, J., Da Cruz, S.,
645   Cleveland, D.W., 2019. Cytoplasmic TDP-43 De-mixing Independent of Stress
646   Granules Drives Inhibition of Nuclear Import, Loss of Nuclear TDP-43, and Cell
647   Death. Neuron 102, 339-357.e7. https://doi.org/10.1016/j.neuron.2019.02.038
648 Goodman, C.A., Pierre, P., Hornberger, T.A., 2012. Imaging of protein synthesis with
649   puromycin. Proc. Natl. Acad. Sci. U.S.A. 109, E989; author reply E990.
650   https://doi.org/10.1073/pnas.1202000109
651 Han, T.W., Kato, M., Xie, S., Wu, L.C., Mirzaei, H., Pei, J., Chen, M., Xie, Y., Allen, J.,
652   Xiao, G., McKnight, S.L., 2012. Cell-free formation of RNA granules: bound RNAs
653   identify features and components of cellular assemblies. Cell 149, 768–779.
654   https://doi.org/10.1016/j.cell.2012.04.016

He, J., Chen, Y., Cai, L., Li, Z., Guo, X., 2018. UBAP2L silencing inhibits cell proliferation and G2/M phase transition in breast cancer. Breast Cancer 25, 224–232. https://doi.org/10.1007/s12282-017-0820-x

Hell, S.W., Wichmann, J., 1994. Breaking the diffraction resolution limit by stimulated emission: stimulated-emission-depletion fluorescence microscopy. Opt Lett 19, 780–782.

Huang, C., Chen, Y., Dai, H., Zhang, Huan, Xie, M., Zhang, Hanbin, Chen, F., Kang, X., Bai, X., Chen, Z., 2019. UBAP2L arginine methylation by PRMT1 modulates stress granule assembly. Cell Death & Differentiation 1. https://doi.org/10.1038/s41418-019-0350-5

Jain, S., Wheeler, J.R., Walters, R.W., Agrawal, A., Barsic, A., Parker, R., 2016. ATPase modulated stress granules contain a diverse proteome and substructure. Cell 164, 487–498. https://doi.org/10.1016/j.cell.2015.12.038

Kato, M., Han, T.W., Xie, S., Shi, K., Du, X., Wu, L.C., Mirzaei, H., Goldsmith, E.J., Longgood, J., Pei, J., Grishin, N.V., Frantz, D.E., Schneider, J.W., Chen, S., Li, L., Sawaya, M.R., Eisenberg, D., Tycko, R., McKnight, S.L., 2012. Cell-free Formation of RNA Granules: Low Complexity Sequence Domains Form Dynamic Fibers within Hydrogels. Cell 149, 753–767. https://doi.org/10.1016/j.cell.2012.04.017

Kedersha, N., Cho, M.R., Li, W., Yacono, P.W., Chen, S., Gilks, N., Golan, D.E., Anderson, P., 2000. Dynamic shuttling of TIA-1 accompanies the recruitment of mRNA to mammalian stress granules. J. Cell Biol. 151, 1257–1268.

Kedersha, N., Panas, M.D., Achorn, C.A., Lyons, S., Tisdale, S., Hickman, T., Thomas, M., Lieberman, J., McInerney, G.M., Ivanov, P., Anderson, P., 2016. G3BP–Caprin1–USP10 complexes mediate stress granule condensation and associate with 40S subunits. The Journal of Cell Biology 212, 845–860. https://doi.org/10.1083/jcb.201508028

Kedersha, N., Tisdale, S., Hickman, T., Anderson, P., 2008. Real-time and quantitative imaging of mammalian stress granules and processing bodies. Meth. Enzymol. 448, 521–552. https://doi.org/10.1016/S0076-6879(08)02626-8

Klar, T.A., Hell, S.W., 1999. Subdiffraction resolution in far-field fluorescence microscopy. Opt Lett 24, 954–956.

Krouwels, I.M., Wiesmeijer, K., Abraham, T.E., Molenaar, C., Verwoerd, N.P., Tanke, H.J., Dirks, R.W., 2005. A glue for heterochromatin maintenance: stable SUV39H1 binding to heterochromatin is reinforced by the SET domain. J. Cell Biol. 170, 537–549. https://doi.org/10.1083/jcb.200502154

Li, D., Huang, Y., 2014. Knockdown of ubiquitin associated protein 2-like inhibits the growth and migration of prostate cancer cells. Oncol. Rep. 32, 1578–1584. https://doi.org/10.3892/or.2014.3360

Li, Q., Wang, W., Hu, Y.-C., Yin, T.-T., He, J., 2018. Knockdown of Ubiquitin Associated Protein 2-Like (UBAP2L) Inhibits Growth and Metastasis of Hepatocellular Carcinoma. Med. Sci. Monit. 24, 7109–7118. https://doi.org/10.12659/MSM.912861

Li, Y.R., King, O.D., Shorter, J., Gitler, A.D., 2013. Stress granules as crucibles of ALS pathogenesis. J. Cell Biol. 201, 361–372. https://doi.org/10.1083/jcb.201302044

Lonsdale, J., Thomas, J., Salvatore, M., Phillips, R., Lo, E., Shad, S., Hasz, R., Walters, G., Garcia, F., Young, N., Foster, B., Moser, M., Karasik, E., Gillard, B., Ramsey, K., Sullivan, S., Bridge, J., Magazine, H., Syron, J., Fleming, J., Siminoff, L., Traino, H., Mosavel, M., Barker, L., Jewell, S., Rohrer, D., Maxim, D., Filkins, D., Harbach, P., Cortadillo, E., Berghuis, B., Turner, L., Hudson, E., Feenstra, K., Sobin, L., Robb, J., Branton, P., Korzeniewski, G., Shive, C., Tabor, D., Qi, L., Groch, K., Nampally, S., Buia, S., Zimmerman, A., Smith, A., Burges, R., Robinson, K., Valentino, K., Bradbury, D., Cosentino, M., Diaz-Mayoral, N., Kennedy, M., Engel,

706   T., Williams, P., Erickson, K., Ardlie, K., Winckler, W., Getz, G., DeLuca, D.,
707   MacArthur, D., Kellis, M., Thomson, A., Young, T., Gelfand, E., Donovan, M., Meng,
708   Y., Grant, G., Mash, D., Marcus, Y., Basile, M., Liu, J., Zhu, J., Tu, Z., Cox, N.J.,
709   Nicolae, D.L., Gamazon, E.R., Im, H.K., Konkashbaev, A., Pritchard, J., Stevens,
710   M., Flutre, T., Wen, X., Dermitzakis, E.T., Lappalainen, T., Guigo, R., Monlong, J.,
711   Sammeth, M., Koller, D., Battle, A., Mostafavi, S., McCarthy, M., Rivas, M., Maller,
712   J., Rusyn, I., Nobel, A., Wright, F., Shabalin, A., Feolo, M., Sharopova, N., Sturcke,
713   A., Paschal, J., Anderson, J.M., Wilder, E.L., Derr, L.K., Green, E.D., Struewing,
714   J.P., Temple, G., Volpi, S., Boyer, J.T., Thomson, E.J., Guyer, M.S., Ng, C.,
715   Abdallah, A., Colantuoni, D., Insel, T.R., Koester, S.E., Little, A.R., Bender, P.K.,
716   Lehner, T., Yao, Y., Compton, C.C., Vaught, J.B., Sawyer, S., Lockhart, N.C.,
717   Demchok, J., Moore, H.F., 2013. The Genotype-Tissue Expression (GTEx) project.
718   Nature Genetics 45, 580–585. https://doi.org/10.1038/ng.2653
719 Mahboubi, H., Stochaj, U., 2017. Cytoplasmic stress granules: Dynamic modulators of cell
720   signaling and disease. Biochimica et Biophysica Acta (BBA) - Molecular Basis of
721   Disease 1863, 884–895. https://doi.org/10.1016/j.bbadis.2016.12.022
722 Markmiller, S., Soltanieh, S., Server, K.L., Mak, R., Jin, W., Fang, M.Y., Luo, E.-C., Krach,
723   F., Yang, D., Sen, A., Fulzele, A., Wozniak, J.M., Gonzalez, D.J., Kankel, M.W.,
724   Gao, F.-B., Bennett, E.J., Lécuyer, E., Yeo, G.W., 2018. Context-Dependent and
725   Disease-Specific Diversity in Protein Interactions within Stress Granules. Cell 172,
726   590-604.e13. https://doi.org/10.1016/j.cell.2017.12.032
727 Martino, L., Morchoisne-Bolhy, S., Cheerambathur, D.K., Van Hove, L., Dumont, J., Joly,
728   N., Desai, A., Doye, V., Pintard, L., 2017. Channel Nucleoporins Recruit PLK-1 to
729   Nuclear Pore Complexes to Direct Nuclear Envelope Breakdown in C. elegans.
730   Dev. Cell 43, 157-171.e7. https://doi.org/10.1016/j.devcel.2017.09.019
731 Matsuki, H., Takahashi, M., Higuchi, M., Makokha, G.N., Oie, M., Fujii, M., 2013. Both
732   G3BP1 and G3BP2 contribute to stress granule formation. Genes Cells 18, 135–
733   146. https://doi.org/10.1111/gtc.12023
734 Mazroui, R., Huot, M.-E., Tremblay, S., Filion, C., Labelle, Y., Khandjian, E.W., 2002.
735   Trapping of messenger RNA by Fragile X Mental Retardation protein into
736   cytoplasmic granules induces translation repression. Hum. Mol. Genet. 11, 3007–
737   3017.
738 Melé, M., Ferreira, P.G., Reverter, F., DeLuca, D.S., Monlong, J., Sammeth, M., Young,
739   T.R., Goldmann, J.M., Pervouchine, D.D., Sullivan, T.J., Johnson, R., Segrè, A.V.,
740   Djebali, S., Niarchou, A., Consortium, T.Gte., Wright, F.A., Lappalainen, T., Calvo,
741   M., Getz, G., Dermitzakis, E.T., Ardlie, K.G., Guigó, R., 2015. The human
742   transcriptome across tissues and individuals. Science 348, 660–665.
743   https://doi.org/10.1126/science.aaa0355
744 Mokas, S., Mills, J.R., Garreau, C., Fournier, M.-J., Robert, F., Arya, P., Kaufman, R.J.,
745   Pelletier, J., Mazroui, R., 2009. Uncoupling Stress Granule Assembly and
746   Translation Initiation Inhibition. Mol Biol Cell 20, 2673–2683.
747   https://doi.org/10.1091/mbc.E08-10-1061
748 Mollet, S., Cougot, N., Wilczynska, A., Dautry, F., Kress, M., Bertrand, E., Weil, D., 2008.
749   Translationally Repressed mRNA Transiently Cycles through Stress Granules
750   during Stress. Mol Biol Cell 19, 4469–4479. https://doi.org/10.1091/mbc.E08-05-
751   0499
752 Panas, M.D., Ivanov, P., Anderson, P., 2016. Mechanistic insights into mammalian stress
753   granule dynamics. J Cell Biol 215, 313–323. https://doi.org/10.1083/jcb.201609081
754 Pichon, X., Bastide, A., Safieddine, A., Chouaib, R., Samacoits, A., Basyuk, E., Peter, M.,
755   Mueller, F., Bertrand, E., 2016. Visualization of single endogenous polysomes

24

reveals the dynamics of translation in live human cells. J. Cell Biol. 214, 769–781. https://doi.org/10.1083/jcb.201605024

Protter, D.S.W., Parker, R., 2016. Principles and Properties of Stress Granules. Trends Cell Biol. 26, 668–679. https://doi.org/10.1016/j.tcb.2016.05.004

Ramaswami, M., Taylor, J.P., Parker, R., 2013. Altered ribostasis: RNA-protein granules in degenerative disorders. Cell 154, 727–736. https://doi.org/10.1016/j.cell.2013.07.038

Schmidt, E.K., Clavarino, G., Ceppi, M., Pierre, P., 2009. SUnSET, a nonradioactive method to monitor protein synthesis. Nat. Methods 6, 275–277. https://doi.org/10.1038/nmeth.1314

Somasekharan, S.P., El-Naggar, A., Leprivier, G., Cheng, H., Hajee, S., Grunewald, T.G.P., Zhang, F., Ng, T., Delattre, O., Evdokimova, V., Wang, Y., Gleave, M., Sorensen, P.H., 2015. YB-1 regulates stress granule formation and tumor progression by translationally activating G3BP1. J Cell Biol 208, 913–929. https://doi.org/10.1083/jcb.201411047

Souquere, S., Mollet, S., Kress, M., Dautry, F., Pierron, G., Weil, D., 2009. Unravelling the ultrastructure of stress granules and associated P-bodies in human cells. J. Cell. Sci. 122, 3619–3626. https://doi.org/10.1242/jcs.054437

Stavreva, D.A., McNally, J.G., 2004. Fluorescence recovery after photobleaching (FRAP) methods for visualizing protein dynamics in living mammalian cell nuclei. Meth. Enzymol. 375, 443–455.

Stoecklin, G., Stubbs, T., Kedersha, N., Wax, S., Rigby, W.F.C., Blackwell, T.K., Anderson, P., 2004. MK2-induced tristetraprolin:14-3-3 complexes prevent stress granule association and ARE-mRNA decay. EMBO J. 23, 1313–1324. https://doi.org/10.1038/sj.emboj.7600163

Tourrière, H., Chebli, K., Zekri, L., Courselaud, B., Blanchard, J.M., Bertrand, E., Tazi, J., 2003. The RasGAP-associated endoribonuclease G3BP assembles stress granules. J. Cell Biol. 160, 823–831. https://doi.org/10.1083/jcb.200212128

Treeck, B.V., Protter, D.S.W., Matheny, T., Khong, A., Link, C.D., Parker, R., 2018. RNA self-assembly contributes to stress granule formation and defining the stress granule transcriptome. PNAS 115, 2734–2739. https://doi.org/10.1073/pnas.1800038115

Uhlén, M., Fagerberg, L., Hallström, B.M., Lindskog, C., Oksvold, P., Mardinoglu, A., Sivertsson, Å., Kampf, C., Sjöstedt, E., Asplund, A., Olsson, I., Edlund, K., Lundberg, E., Navani, S., Szigyarto, C.A.-K., Odeberg, J., Djureinovic, D., Takanen, J.O., Hober, S., Alm, T., Edqvist, P.-H., Berling, H., Tegel, H., Mulder, J., Rockberg, J., Nilsson, P., Schwenk, J.M., Hamsten, M., von Feilitzen, K., Forsberg, M., Persson, L., Johansson, F., Zwahlen, M., von Heijne, G., Nielsen, J., Pontén, F., 2015. Proteomics. Tissue-based map of the human proteome. Science 347, 1260419. https://doi.org/10.1126/science.1260419

van der Laan, A.M.A., van Gemert, A.M.C., Dirks, R.W., Noordermeer, J.N., Fradkin, L.G., Tanke, H.J., Jost, C.R., 2012. mRNA cycles through hypoxia-induced stress granules in live Drosophila embryonic muscles. Int. J. Dev. Biol. 56, 701–709. https://doi.org/10.1387/ijdb.103172al

Vilas-Boas, F. de A.S., da Silva, A.M., de Sousa, L.P., Lima, K.M., Vago, J.P., Bittencourt, L.F.F., Dantas, A.E., Gomes, D.A., Vilela, M.C., Teixeira, M.M., Barcelos, L.S., 2016. Impairment of stress granule assembly via inhibition of the eIF2alpha phosphorylation sensitizes glioma cells to chemotherapeutic agents. J. Neurooncol. 127, 253–260. https://doi.org/10.1007/s11060-015-2043-3

Weber, S.C., Brangwynne, C.P., 2012. Getting RNA and protein in phase. Cell 149, 1188–1191. https://doi.org/10.1016/j.cell.2012.05.022

807 Wheeler, J.R., Matheny, T., Jain, S., Abrisch, R., Parker, R., 2016. Distinct stages in stress
808   granule assembly and disassembly. Elife 5. https://doi.org/10.7554/eLife.18413
809 Ye, T., Xu, J., Du, L., Mo, W., Liang, Y., Xia, J., 2017. Downregulation of UBAP2L Inhibits
810   the Epithelial-Mesenchymal Transition via SNAIL1 Regulation in Hepatocellular
811   Carcinoma Cells. Cell. Physiol. Biochem. 41, 1584–1595.
812   https://doi.org/10.1159/000470824
813 Youn, J.-Y., Dunham, W.H., Hong, S.J., Knight, J.D.R., Bashkurov, M., Chen, G.I., Bagci,
814   H., Rathod, B., MacLeod, G., Eng, S.W.M., Angers, S., Morris, Q., Fabian, M., Côté,
815   J.-F., Gingras, A.-C., 2018. High-Density Proximity Mapping Reveals the
816   Subcellular Organization of mRNA-Associated Granules and Bodies. Molecular Cell
817   69, 517-532.e11. https://doi.org/10.1016/j.molcel.2017.12.020
818 Zhao, B., Zong, G., Xie, Y., Li, J., Wang, H., Bian, E., 2015. Downregulation of ubiquitin-
819   associated protein 2-like with a short hairpin RNA inhibits human glioma cell growth
820   in vitro. Int. J. Mol. Med. 36, 1012–1018. https://doi.org/10.3892/ijmm.2015.2323
821

822 FIGURE LEGENDS

823 **Figure 1. Inside stress granules UBAP2L forms discrete particles that do not**
824 **colocalize with G3BP cores.**

825 A) 3D-STED images of a stress granule (detected by anti-UBAP2L or anti-G3BP staining)
826 in HeLa K cells treated with 0.1 mM arsenite for 30 minutes prior to fixation. Scale bars
827 correspond to 0.5 µm.

828 B) Size distribution of stress granule particles of UBAP2L and G3BP.

829 C) Representative images over time of a FRAP experiment on UBAP2L-mScarlet HeLa cells
830 treated with 0.5 mM arsenite. White circle represents the bleached area. Time is expressed
831 at mm:ss and indicated on the image, top left. Scale bars correspond to 10 µm. The red
832 dotted line centered at 1 highlights complete fluorescence recovery.

833 D) Average FRAP recovery curves of the first FRAP cycle and the second FRAP cycle.
834 Mean ± 95% Confidence Interval (C.I.), n= 27 stress granules from 27 cells.

835 E) Deconvolved 2D-STED images of a stress granule in HeLa K cells treated with 0.1 mM
836 arsenite. Cells were stained with anti-UBAP2L and anti-G3BP antibodies. Scale bar
837 corresponds to 1 µm.

838 F) Line profile of the region of interest (ROI) highlighted by the white boxes in (E). The two
839 top panels represent the magnification of the ROI split into two channels: UBAP2L (Cyan)
840 and G3BP (Magenta). The graph corresponds to the normalized pixel-by-pixel gray value of
841 the two images above.

842 G) Left: Deconvolved 3D confocal image of U-ExM of a stress granule in HeLa K cells treated
843 30 minutes with 0.1 mM arsenite and stained with anti-UBAP2L and anti-G3BP antibodies.
844 Right: 3D reconstruction of the surface of UBAP2L (Cyan) and G3BP (Magenta) particles.

H) Deconvolved 3D confocal image of U-ExM of a stress granule in HeLa K cells treated 30 minutes with 0.1 mM arsenite, stained with anti-UBAP2L and anti-G3BP antibodies.

I) Line profile of the ROI highlighted by the white boxes in (G). The two top panels represent the magnification of the ROI split into two channels: UBAP2L (Cyan) and G3BP (Magenta). The graph corresponds to the normalized pixel-by-pixel gray value of the two images above.

Figure Supplementary 1. Development of a UBAP2L-mScarlet HeLa cell line.

A) Linear regression of stress granule size measured by 3D-STED versus the number of particles per granule.

B) Schematic representation and screening strategy used to identify UBAP2L-mScarlet fusion clones.

C) Representative image of PCR products of parental HeLa cells compared to a clone with successful mScarlet insertion, as indicated.

D) Image of a Western blot of lysates from HeLa K cells (left) compared to HeLa UBAP2L-mScarlet cells (right). In both (D) and (E) the membrane was blotted with anti-UBAP2L (upper panel), and anti-Tubulin (lower panel) antibodies.

E) Image of a Western blot of lysates from HeLa UBAP2L-mScarlet cells treated with different siRNAs.

F) Maximum projections of wide-field images from time-lapse movies of HeLa UBAP2L-mScarlet cells non treated (NT) and treated with 0.5 mM arsenite. Time is expressed at hh:mm, top left of each image. Scale bar corresponds to 10 μm.

G) Graph showing the FRAP recovery of the first FRAP cycle and the second FRAP cycle of all the cells analyzed in Fig. 1 D. The continuous lines represent the single exponential functions used to fit the mean of the recovery curves. The red dotted line centered at 1 highlights complete fluorescence recovery.

H) Histogram representing the percentage of mobile fraction (MF) and immobile fraction (IF) in the two FRAP cycles. Error bars indicate SD. Statistical significance was determined using ANOVA and Dunnett's multiple comparison.

Figure 2. UBAP2L localizes to and is required for stress granule formation after exposure to diverse stress conditions.

A) Confocal images of HeLa K cells stained with anti-G3BP and anti-UBAP2L antibodies and counterstained with DAPI. In all figures, NT is non-treated cells. White box indicates the

878 ROI enlarged and depicted in separate channels on the top right. The scale bar in the main

879 image corresponds to 10 μm, the scale bar in the ROI corresponds to 1 μm.

880 B) Scatterplot representing the cross correlation between G3BP1 and UBAP2L signal. Error

881 bars indicate SD. Statistical significance was determined using ANOVA and Dunnett's

882 multiple comparison. Each dot corresponds to the Pearson coefficient of a single ROI. N =

883 3 independent experiments. In all figures and supplementary figures, ns, p > 0.05, ∗p < 0.05,

884 ∗∗p < 0.01, ∗∗∗p < 0.001, ∗∗∗∗p < 0.0001.

885 C) Maximum projections of confocal images of HeLa K cells transfected with the indicated

886 siRNAs, stained with anti-G3BP and anti-UBAP2L antibodies and counterstained with DAPI.

887 Scale bar corresponds to 10 μm.

888 D) Percentage of HeLa K cells transfected with the indicated siRNAs containing G3BP1-

889 positive stress granules. Error bars indicate Standard Error of the Mean (SEM). Statistical

890 significance was determined using two-way ANOVA and Tukey's multiple comparison. N ≥

891 2 independent experiments.

892

893 **Figure Supplementary 2. UBAP2 colocalizes with G3BP1 in arsenite-induced stress**

894 **granules and it is required for stress granules assembly.**

895 A) Left: Confocal images of HeLa K cells stained with anti-G3BP and anti-UBAP2L

896 antibodies and counterstained with DAPI. Cells were either non treated (first row) or treated

897 with sodium arsenite 0.1 mM for 30 min (second row). Scale bar corresponds to 10 μm.

898 Right: magnification of a ROI of the images on the left (white box). Scale bars correspond

899 to 1 μm.

900 B) Cross correlation between G3BP and UBAP2L signal before and after a 90° rotation of

901 the image. Each dot corresponds to the Pearson coefficient of a single ROI. Error bars

902 indicate SD. 82 (Control) and 100 (arsenite) cytoplasmic ROIs from 3 independent

903 experiments were analyzed.

904 C) Representative image of a Western blot of lysates from HeLa K cells transfected with a

905 control siRNA (first lane) compared to lysates of HeLa K transfected with a siRNAs targeting

906 UBAP2L (2nd and 3rd lane). The membrane was blotted with anti-UBAP2L and anti-αTubulin,

907 as indicated.

908 D) Percentage of UBAP2L depletion in HeLa K cells treated with the indicated siRNAs,

909 quantified from western blots. Error bars indicate Standard Error of the Mean (SEM).

910 Statistical significance was determined using ANOVA and Dunnett's multiple comparison.

911 N=4 independent experiments.

912 E) Maximum projections of confocal images of HeLa K cells transfected with the indicated

913 siRNAs and stained with different stress granule markers. Cells treated for 30 minutes with

914 0.1 mM arsenite or left untreated. Left: anti-G3BP and anti-TIA1 antibodies and

915 counterstained with DAPI. Right: anti-G3BP and anti-USP10 antibodies and counterstained

916 with DAPI. Scale bars correspond to 10 µm.

917

918 **Figure 3. Recruitment of UBAP2L to stress granules is independent of G3BP.**

919 A) Maximum projections of confocal images of HeLa K cells transfected with the indicated

920 siRNAs and stained with anti-G3BP, anti-UBAP2L antibodies and counterstained with DAPI.

921 Cells were either left untreated (upper panels), treated with 0.1 mM arsenite for 30 minutes

922 (lower panels). White box indicates the ROI endlarged and depicted in separate channels

923 on the bottom left. Scale bar in the image corresponds to 10 µm, scale bar in the ROI

924 corresponds to 2 µm.

925 B) Percentage of HeLa cells transfected with the indicated siRNA, containing either UBAP2L

926 positive stress granules or G3BP1 positive stress granules. Cells were treated with arsenite

927 0.1 mM or left untreated. N≥2 independent experiments. Statistical significance was

928 determined using two-way ANOVA and Tukey's multiple comparison.

929 C) Maximum projections of confocal images of U2OS and U2OS ΔΔG3BP1/2 cells stained

930 with anti-G3BP and anti-UBAP2L antibodies and counterstained with DAPI. Cells were

931 either left untreated (top) or treated 60 minutes with 0.1 mM arsenite (bottom). White box

932 highlights the ROI corresponding to the detail enlarged in the bottom left of the image. Scale

933 bar in the image corresponds to 10 µm. Scale bar in the detail corresponds to 2 µm.

934 D) Percentage of U2OS, U2OS ΔG3BP1, U2OS ΔG3BP2, U2OS ΔΔG3BP1/2 cells

935 containing either UBAP2L positive stress granules or G3BP1 positive stress granules after

936 60 minutes exposure to 0.1 mM arsenite. N=3 independent experiments. Statistical

937 significance was determined using two-way ANOVA and Tukey's multiple comparison.

938 E) Quantification of UBAP2L-positive stress granule areas in HeLa K cells transfected with

939 the indicated siRNA and treated 30 minutes with 0.1 mM arsenite. Mean ± SEM. Each dot

940 represents an independent experiment. Statistical significance was determined using two-

941 way ANOVA and Dunnett's multiple comparison.

942 F) Quantification of UBAP2L-positive stress granule areas in U2OS, U2OS ΔG3BP1, U2OS

943 ΔG3BP2, U2OS ΔΔG3BP1/2 cells, 60 minutes after 0.1 mM arsenite treatment. Mean ±

944 SEM. Each dot represents an independent experiment. Statistical significance was

945 determined using two-way ANOVA and Dunnett's multiple comparison.

Figure Supplementary 3. Depletion of G3BP1 and 2.
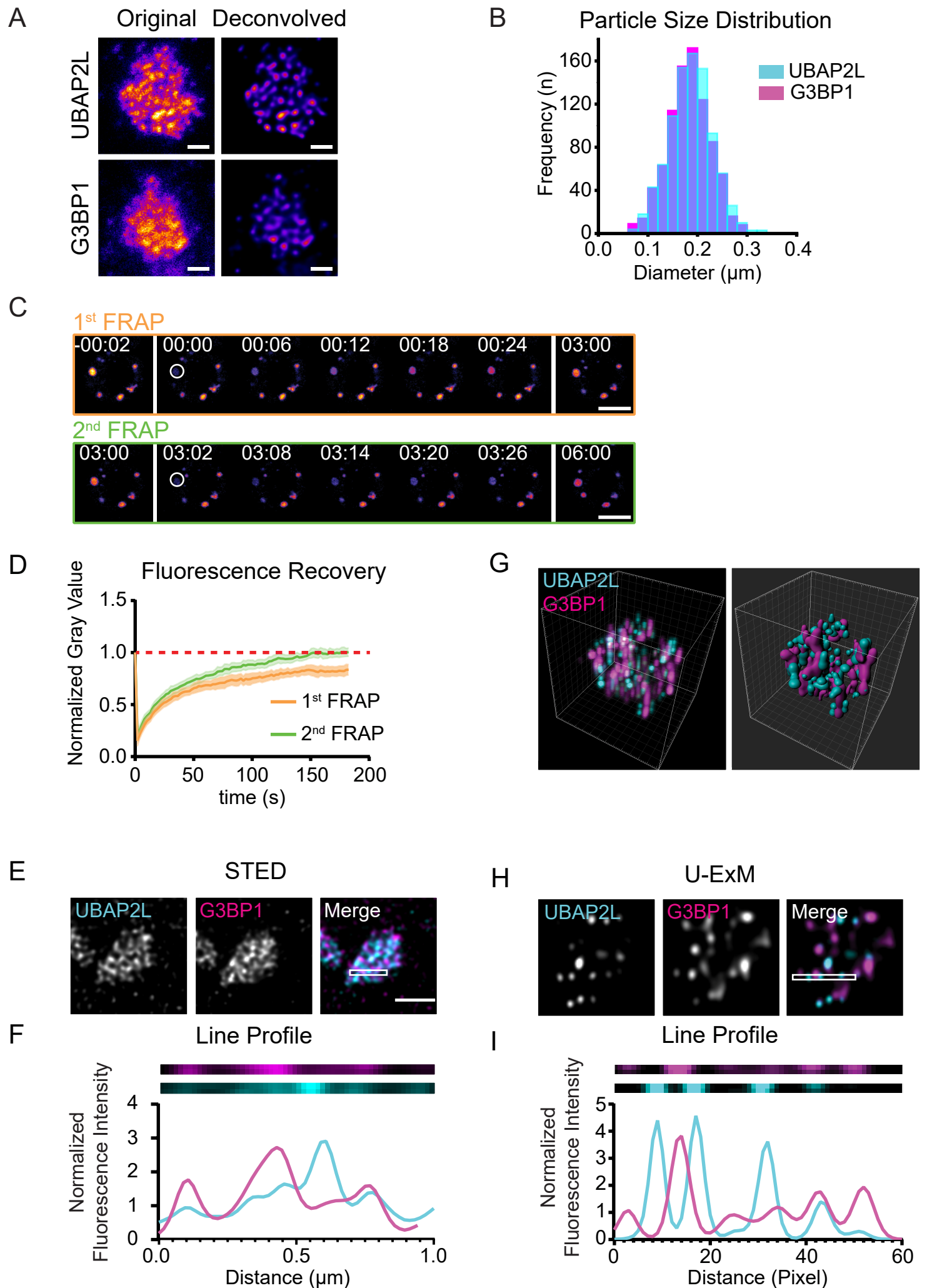
Image of a Western blot of lysates from HeLa K cells transfected with a control siRNA (1st lane) compared to lysates of HeLa K transfected with a siRNAs targeting G3BP1 and 2 (2nd, 3rd and 4th lane). The membrane was blotted with anti-G3BP, anti-G3BP2 and anti-PCNA (loading control) antibodies as indicated.

Figure 4. UBAP2L depletion does not affect stress induced translational inhibition.

A) Representative image of a Western blot of lysates from HeLa K cells transfected with a control siRNA (1st and 4th lane) compared to lysates of HeLa K transfected with siRNAs targeting UBAP2L (2nd, 3rd, 5th and 6th lane). Cells where either left untreated (1st, 2nd, 3rd lane) or treated 30 minutes with 0.1 mM arsenite (4th, 5th, 6th lane). The membrane was blotted with anti-UBAP2L, anti-αTubulin, anti-pS51-eIF2α and anti- eIF2α antibodies, as indicated. N=3 independent experiments.

B) Representative image of a Western blot of lysates from HeLa K cells transfected with a control siRNA (1st and 4th lane) compared to lysates of HeLa K transfected with siRNAs targeting UBAP2L (2nd, 3rd, 5th and 6th lane). Cells where either left untreated (1st, 2nd, 3rd lane) or treated 30 minutes with 0.1 mM arsenite (4th, 5th, 6th lane). 10 minutes before lysis cells were incubated with medium supplemented with 10 μg/ml Puromycin. The membrane was blotted with anti-Puromycin and anti-αTubulin as indicated. N=3 independent experiments.
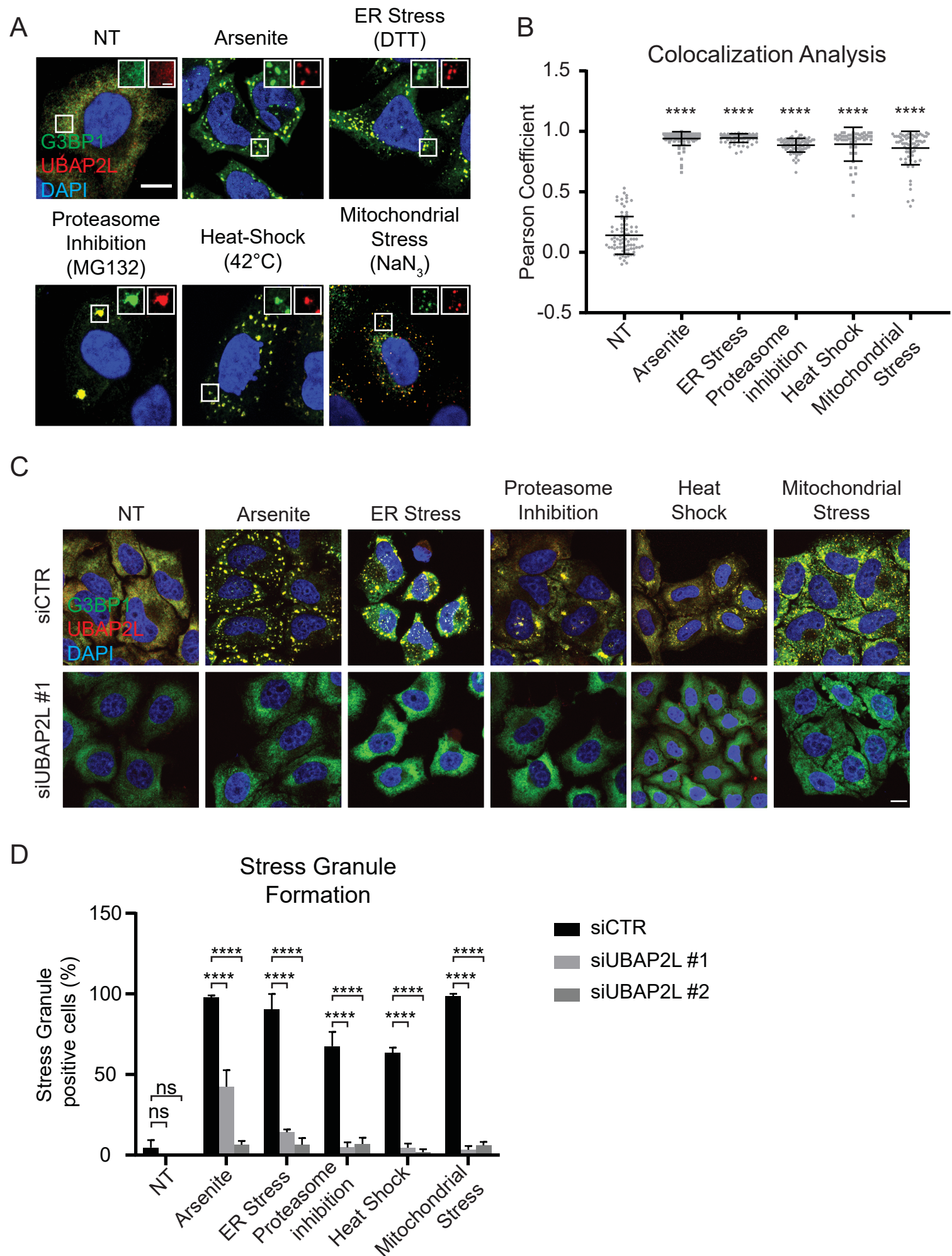
C) Quantification of a polysome decay assay. It is represented the mean normalized polysome density ± SEM over time following addition of 0.1 mM arsenite, or 0.1 mM arsenite and 50 μg/ml Cycloheximide in the culture medium. N=7 independent experiments.
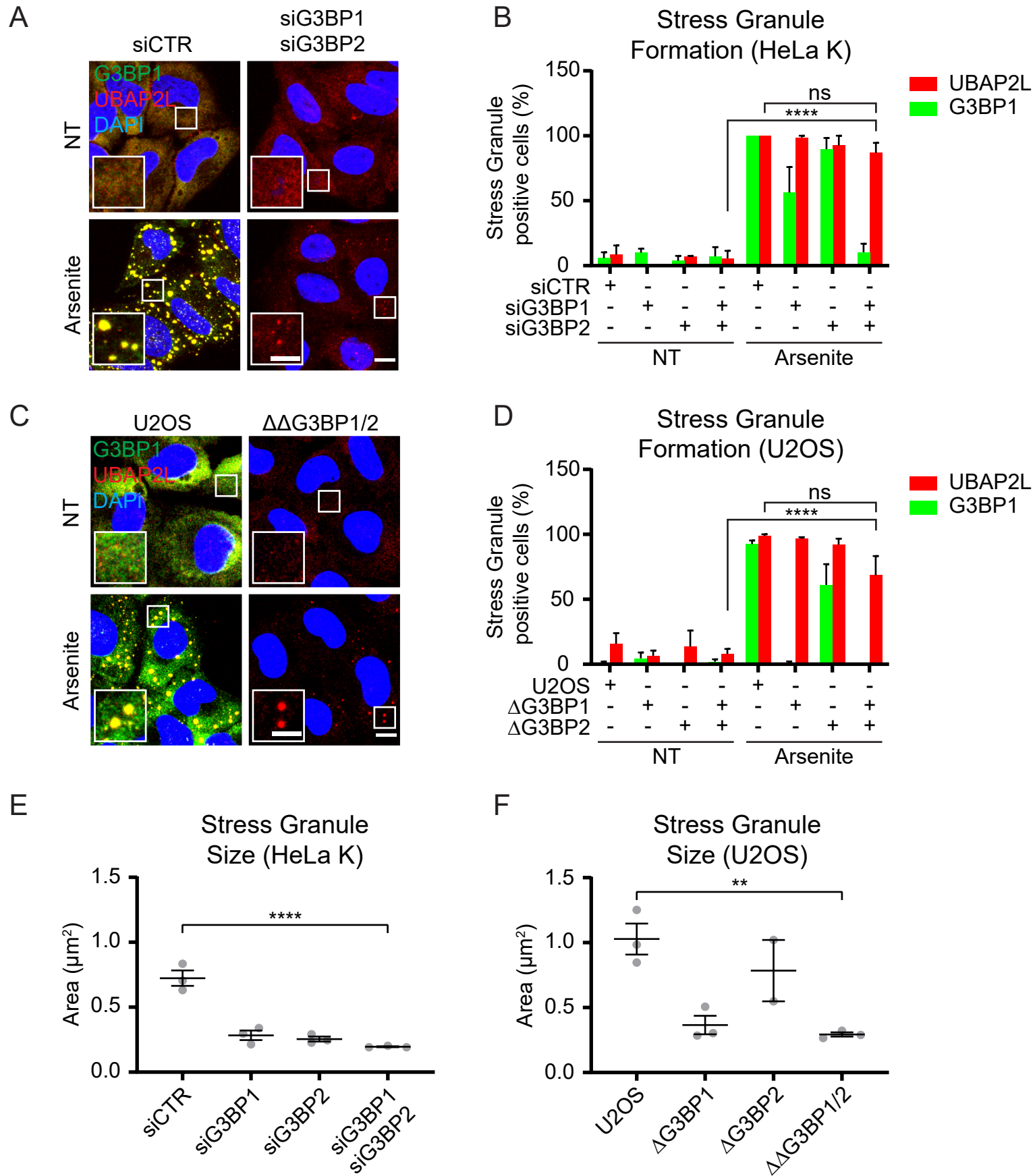
D) Maximum projections of confocal images of HeLa K cells stained with anti-G3BP and anti-UBAP2L antibodies and counterstained with DAPI. Cells were either left untreated (left panel), treated with 0.1 mM arsenite for 30 minutes (middle panel) or treated with both arsenite 0.1 mM and cycloheximide 50 μg/ml for 30 minutes (right panel). Scale bar in the image corresponds to 10 μm.
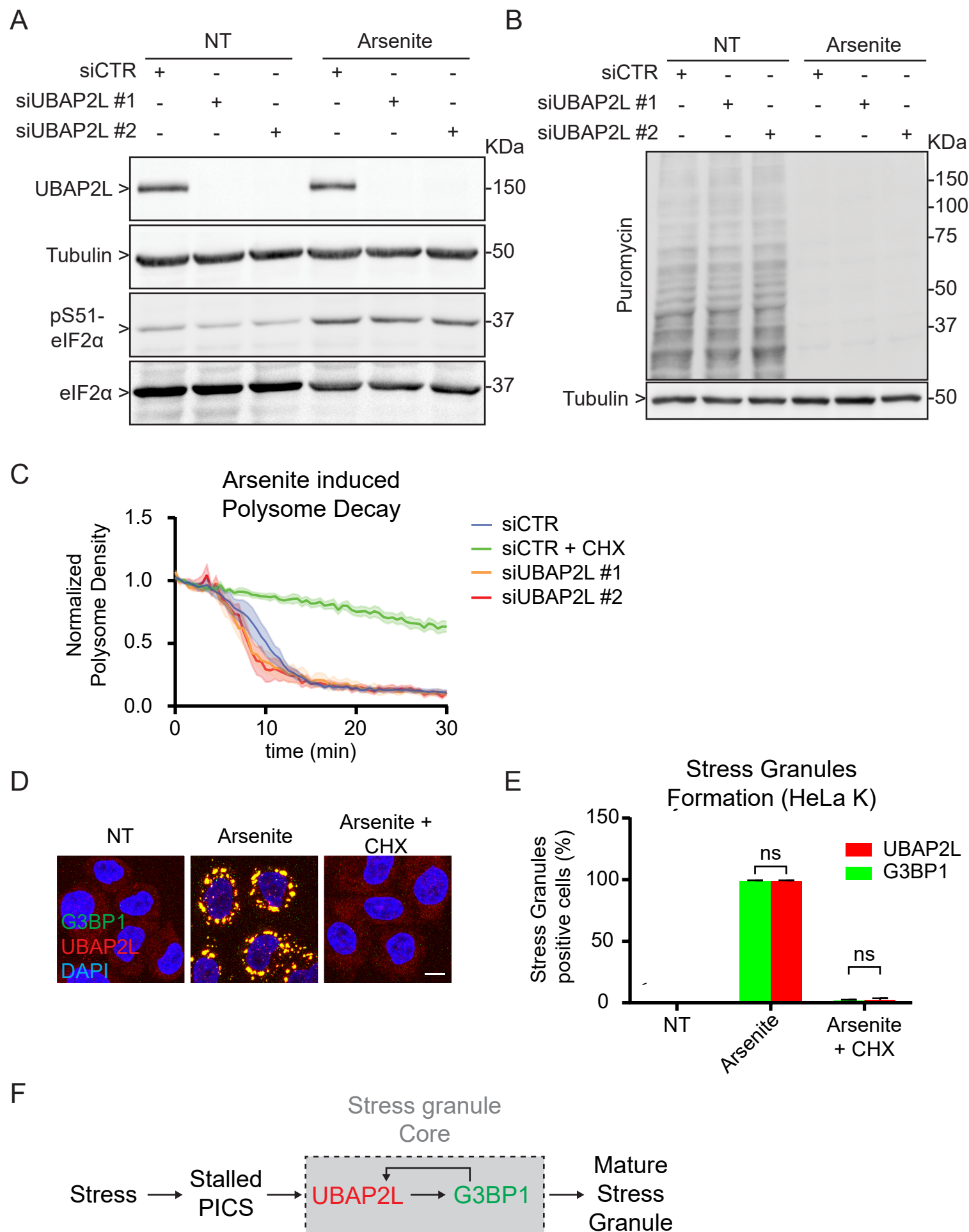
E) Percentage of HeLa cells containing either UBAP2L positive stress granules or G3BP1 positive stress granules in untreated condition, after 30 minutes exposure to arsenite 0.1 mM, or to arsenite 0.1 mM and cycloheximide 50 μg/ml. N=3 independent experiments.
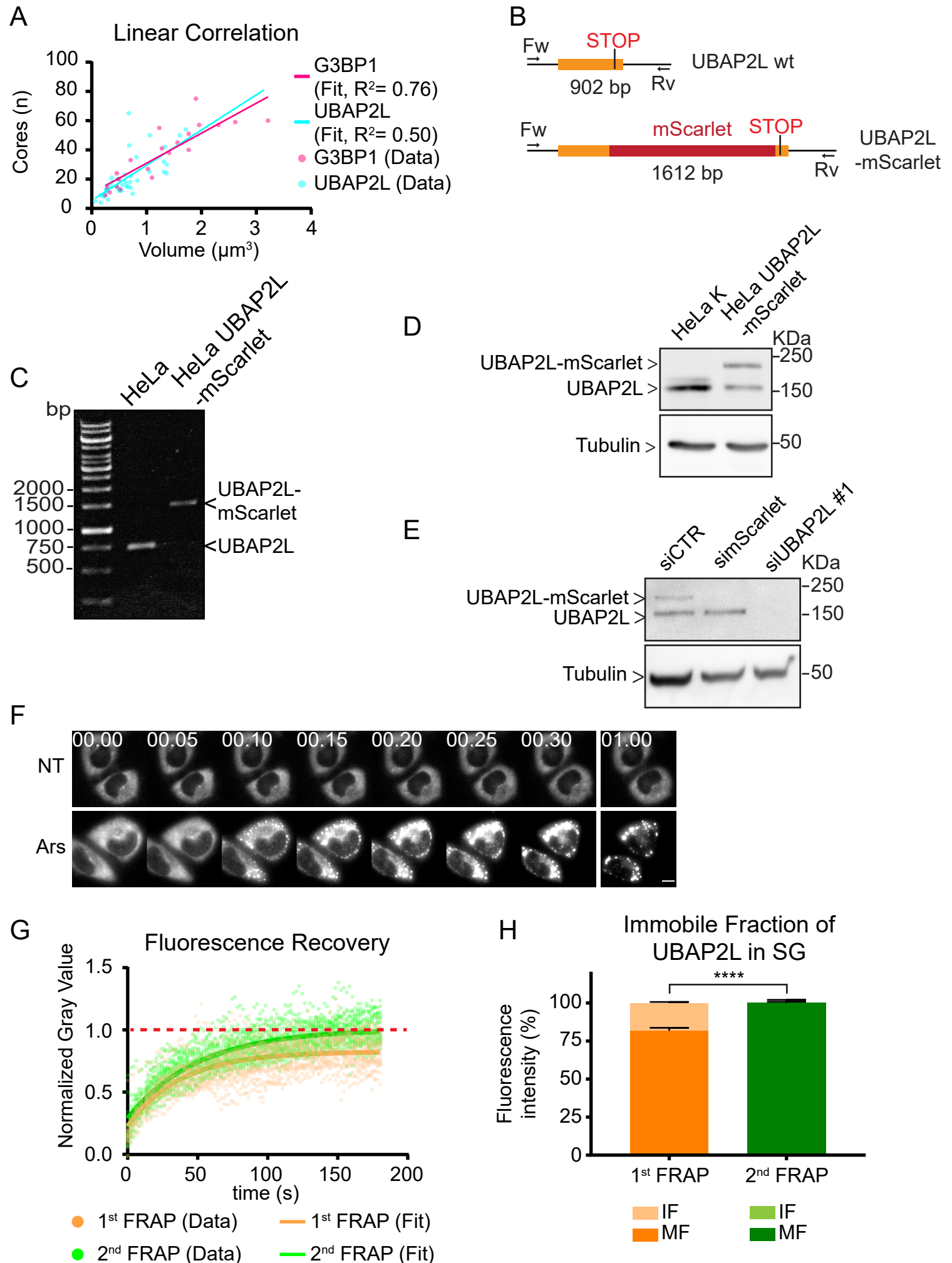
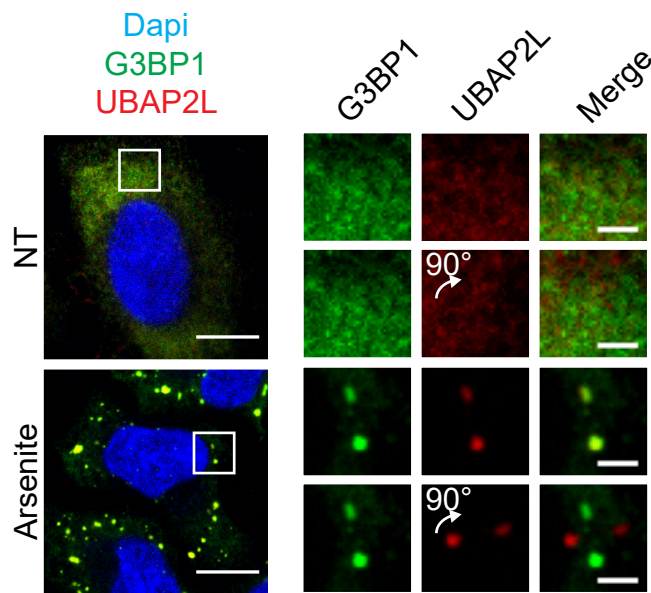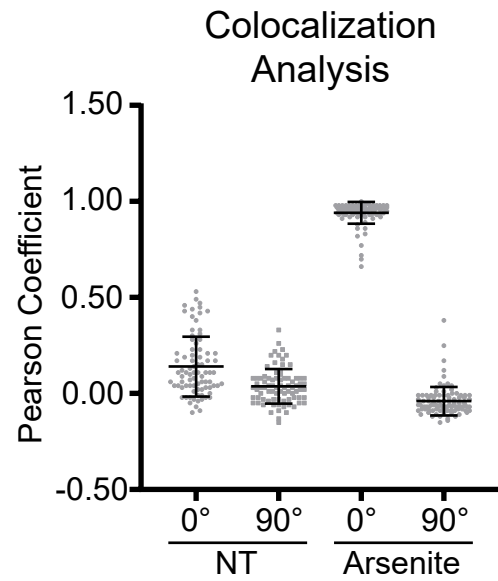F) Schematic drawing of the proposed mechanism for stress granules core formation.
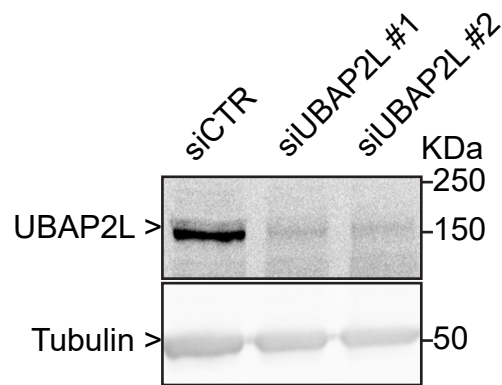
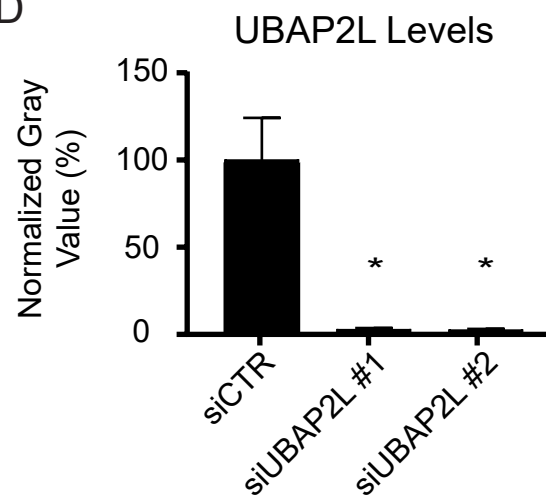# Cirillo et al. Figure

Cirillo et al. Figure 2

Cirillo et al. Figure 3

A

B

C

Arsenite induced Polysome Decay

- siCTR
- siCTR + CHX
- siUBAP2L #1
- siUBAP2L #2

D

E

Stress Granules Formation (HeLa K)

- UBAP2L
- G3BP1

F

Stress → Stalled PICS → [Stress granule Core: UBAP2L → G3BP1] → Mature Stress Granule

Cirillo et al. Figure Supplementary 1

Cirillo et al. Figure Supplementary 3